Structure-specific glial response in a macaque model of neuroAIDS: multivoxel proton magnetic resonance spectroscopic imaging at 3 Tesla

William E. Wu[a], Assaf Tal[a], Ke Zhang[a], James S. Babb[a], Eva-Maria Ratai[b], R. Gilberto González[b] and Oded Gonen[a]

Objective: As ~40% of persons with HIV also suffer neurocognitive decline, we sought to assess metabolic dysfunction in the brains of simian immunodeficiency virus (SIV)-infected rhesus macaques, an advanced animal model, in structures involved in cognitive function. We test the hypothesis that SIV-infection produces proton-magnetic resonance spectroscopic imaging (^{1}H-MRSI)-observed decline in the neuronal marker, N-acetylaspartate (NAA), and elevations in the glial marker, myo-inositol (mI), and associated creatine (Cr) and choline (Cho) in these structures.

Design: Pre- and 4–6 weeks post-SIV infection (with CD8^{+} T-lymphocyte depletion) was monitored with T_2-weighted quantitative MRI and $16 \times 16 \times 4$ multivoxel ^{1}H-MRSI ($TE/TR = 33/1400$ ms) in the brains of five rhesus macaques.

Methods: Exploiting the high-resolution ^{1}H-MRSI grid, we obtained absolute, cerebrospinal fluid partial volume-corrected NAA, Cr, Cho and mI concentrations from centrum semiovale, caudate nucleus, putamen, thalamus and hippocampus regions.

Results: Pre- to post-infection mean Cr increased in the thalamus: 7.2 ± 0.4 to 8.0 ± 0.8 mmol/l (+11%, $P < 0.05$); mI increased in the centrum semiovale: 5.1 ± 0.8 to 6.6 ± 0.8 mmol/l, caudate: 5.7 ± 0.7 to 7.3 ± 0.5 mmol/l, thalamus: 6.8 ± 0.8 to 8.5 ± 0.8 mmol/l and hippocampus: 7.7 ± 1.2 to 9.9 ± 0.4 mmol/l (+29%, +27%, +24% and +29%, all $P < 0.05$). NAA and Cho changes were not significant.

Conclusion: SIV-infection appears to cause brain injury indirectly, through glial activation, while the deep gray matter structures' neuronal cell bodies are relatively spared. Treatment regimens to reduce gliosis may, therefore, prevent neuronal damage and its associated neurocognitive impairment.

© 2013 Wolters Kluwer Health | Lippincott Williams & Wilkins

Introduction

Although HAART has reduced HIV/AIDS-associated mortality and dementia, ~40% of the million-plus infected in the United States will suffer milder, long-term forms of HIV-associated neurocognitive disorders (HAND), which include impairments in memory and executive function that diminish quality-of-life and productivity [1,2]. Overall HAND risk has increased among chronically infected older individuals [3], despite years of HAART [4–6]. Moreover, the attenuated association between plasma RNA viral load and cognitive impairment in treated individuals suggests the underlying pathology may be related to other,

metabolic alterations in central nervous system (CNS) areas [7,8].

Indeed, neuroimaging studies using MRI and proton-magnetic resonance spectroscopy (^{1}H-MRS) have revealed continued structural and metabolic abnormalities in infected individuals even while their viral loads were undetectable [5,9–11]. These often occur subcortically in the basal ganglia, thalamus and white matter, but also in hippocampus, all areas crucial to executive, cognitive and memory functions, and most (with the exception of putamen) periventricular in location. These abnormalities have also been found to correlate with cognitive deficits [9,12]. Histopathology from seropositive patient brains has also confirmed that HIV-1 preferentially targets basal ganglia (especially the caudate nucleus and putamen) [13], thalamus [14], white matter [15] and hippocampus [16–18].

Although HIV affects various brain regions differently, its specific metabolic effects in these CNS structures thought to underlie cognitive dysfunction(s) remain less well characterized. As human studies of CNS involvement can be logistically challenging early on after infection (as most newly infected are unaware of their status) and studies during the advanced stages of neurologic complication can be difficult in a cognitively-impaired group – with potential opportunistic infections exacerbating morbidity to mortality – animal model systems are often used. Simian immunodeficiency virus (SIV)-infected rhesus macaque, in particular, is a well established model system mimicking HIV's development of AIDS, CNS disease, cognitive and behavioral deficits [19–22]. Both the traditional and accelerated (using CD8$^+$ T-lymphocyte depletion) models of study have provided insight into the nature and dynamics of HIV cerebral injury and both have shown similar histopathology at the advanced stage [23–25]. However, past ^{1}H-MRS studies were limited by low, 1–4 cm^3 spatial resolution (relative to the $\sim$80 cm^3 brain) and single voxels that missed more than 95% of the brain and that also suffered gray matter, white matter and cerebrospinal fluid (CSF) partial volume effects, reducing metabolite quantification performance [26].

We address these issues with three-dimensional multi-voxel proton-magnetic resonance spectroscopic imaging (^{1}H-MRSI) at 0.125 cm^3 spatial resolution over substantial, $\sim$35% of the macaque brain [27], volume corrected for CSF partial volume [28]. Using this technique, we previously found global abnormalities suggestive of diffuse pathology in five animals [29]. Histopathology, however, has also revealed regional heterogeneity and variable disease progression, suggesting different disease mechanisms in various regions and that some may be more susceptible than others [25,30]. As the high-spatial resolution ^{1}H-MRSI grid also facilitates post hoc analyses and irregularly shaped region-of-interest definition [31], in this study we test the hypothesis that

SIV-infection may lead to: neuronal damage, reflected by a decrease in the concentration of their N-acetylaspartate (NAA) marker; and glial activation, marked by increased myo-inositol (mI), choline (Cho) and creatine (Cr) [32] in brain regions implicated in memory or cognitive function: the centrum semiovale, caudate, putamen, thalamus and hippocampus. We test these hypotheses in five rhesus macaques, comparing their absolute metabolite levels pre- and several weeks post-infection.

Methods

Nonhuman primates

Five (two females, three males; 5.0–8.6 kg weight) healthy 3–4 year-old rhesus macaques (Macaca mulatta) were scanned under constant veterinary supervision. Each was tranquilized with 15–20 mg/kg intramuscular ketamine hydrochloride and intubated to ensure a patent airway during the experiment (no mechanical ventilation was needed). Intravenous injection of 0.4 mg/kg atropine was used to prevent bradycardia. Continuous infusion of propofol (0.25 mg/kg per min) was maintained via a catheter in a saphenous vein. Heart and respiratory rates, oxygen saturation and end-tidal CO_2 were monitored continuously and a water blanket used to prevent hypothermia. All were subsequently intravenously infected with SIVmac251 virus (10 ng SIVp27) and their CD8$^+$ T-lymphocytes depleted to speed up progression to, and increase the incidences of, terminal AIDS and SIV encephalitis [33,34]. The model yields similar CNS pathology to that of the later, more commonly diagnosed [35] and increasingly more prevalent [1,36] stages of HIV-infection in several weeks instead of years. CD8$^+$ depletion was done with a mouse-human chimeric, monoclonal (cM-T807) antibody targeted against CD8 at 6, 8 and 12 days post-inoculation [37,38]. Previous histopathological and ^{1}H-MRS studies comparing the result of the non-CD8-depleted ('traditional') versus this CD8-depleted ('accelerated') model have shown similar findings at their comparable infection stages [25,33,39]. Two animals were rescanned 4 weeks and three 6 weeks later. The protocol was approved by the Harvard Medical School and Massachusetts General Hospital Institutional Animal Care and Utilization Committees.

MRI data acquisition

All experiments were done in a 3 T whole-body MR imager (Magnetom TIM Trio, Siemens AG, Erlangen, Germany), using its circularly polarized transmit-receive human knee-coil capable of producing a peak 2 kHz (45.2 µT) radio-frequency B_1 field. To guide the ^{1}H-MRSI volume-of-interest (VOI) and for tissue segmentation, sagittal and axial T_2-weighted turbo spin echo (TSE) MRI: $TE/TR = 16/7430$ ms, 140×140 mm^2 field-of-view (FOV), 512×512 matrix, 24 sagittal slices, 2 mm slice thickness and 40 axial slices, 1.2 mm slice thickness, were acquired.

Multivoxel three-dimensional ¹H-MRSI

A 4.0 cm anterior–posterior (AP) × 3.5 cm left–right (LR) × 2.0 cm inferior–superior (IS) = 28 cm³ VOI was image-guided, as shown in Fig. 1 [40]. The VOI was then excited using PRESS ($TE/TR = 33/1440$ ms) with two second-order Hadamard encoded slabs (4 slices)

interleaved along the IS direction every *TR*. This approach optimizes signal-to-noise-ratio (SNR) and spatial coverage [28] and allows a strong, 9 mT/m, slice-selection gradient to keep the 1.6 ppm chemical shift displacement from NAA to *m*I to 0.5 mm, less than 10% of the slice thickness [41].
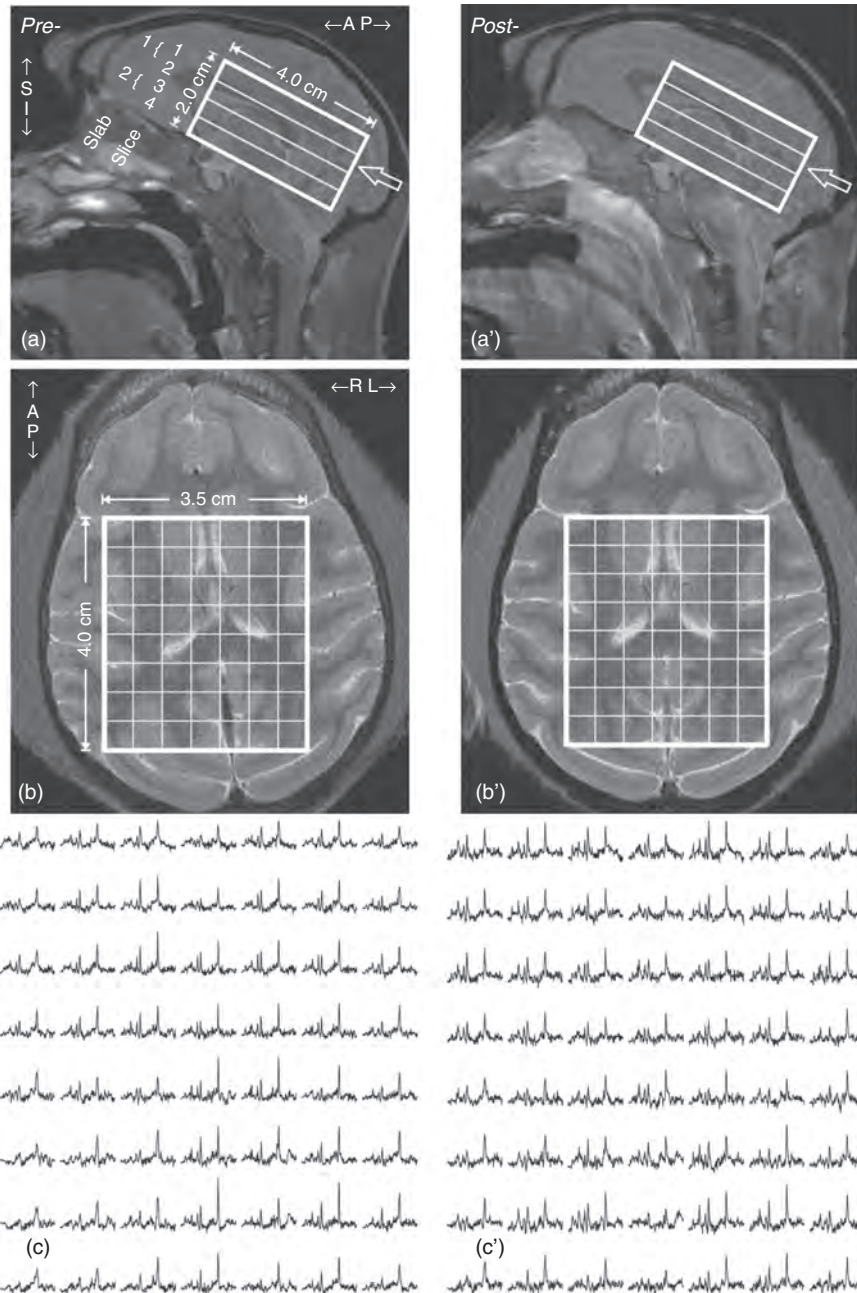

Fig. 1. Top and middle: Sagittal, (a) before and (a′) 4 weeks after SIV infection, and axial (b, b′) T_2-weighted TSE MRI from a female rhesus macaque head *pre*- and *post*-SIV infection showing the location and size of the 3.5 × 4 × 2 cm³ VOI (solid lines), CSI grid and two second-order Hadamard slabs, "1{" and "2{", encoding 1…4 slices in the inferior–superior direction (a). The open arrows on (a) and (a′) denote the axial plane level of (b) and (b′). Note the similar VOI placement, brain coverage and grid resolution that facilitates definition of irregularly-shaped brain structures. **Bottom,** (c, c′): Real part of the 7 × 8 axial ¹H spectra matrix from the VOI on (b, b′). All spectra represent 0.125 cm³ voxels and are on the same frequency and intensity scales. Note the metabolite SNRs and spectral resolution, which led to reliable fits as reflected by mean voxel CRLBs <15% for all four metabolites.

The slices' planes were encoded with 16×16 two-dimensional chemical shift imaging (CSI) over $8 \times 8\,\mathrm{cm}^2$ (LR $\times$ AP) FOV, yielding nominal $(0.5\,\mathrm{cm})^3 = 0.125\,\mathrm{cm}^3$ voxels ($0.55 \times 0.55 \times 0.5\,\mathrm{cm}^3 \approx 0.15\,\mathrm{cm}^3$ given the full-width at half-maximum (FWHM) of the two-dimensional CSI point spread function [42–44]). The VOI was defined in the slices' planes by two 9 ms PRESS $180°$ radio-frequency pulses, under 3.3 and 2.9 mT/m (4.9 kHz bandwidth). The localization grid formed 7×8 voxels in each of the four slices (Fig. 1) for a total of 224 in the VOI. The MRSI signal was acquired for 256 ms with 512 points at ± 1 kHz bandwidth. Each $16 \times 16 \times 4$ scan took 12.5 min and after four averages the entire procedure was ~50 min.

Metabolic quantification

The ^{1}H-MRSI data were processed using in-house software (Integrated Data Language version 6.3; Research Systems Inc., Boulder, Colorado, USA). Residual water signal was removed in the time domain [45]; then the data were Fourier transformed in the time, AP and LR directions and Hadamard reconstructed along the IS direction. Spectra were voxel-shifted to align the CSI grid with the VOI NAA, then corrected automatically for frequency and zero-order phase shifts with reference to the NAA peak in each voxel [40]. Relative levels of the $i =$ NAA, Cr, Cho, mI metabolites in the $j = 1...224$ VOI voxels of the $k = 1...5$ animals, S_{ijk}-s, were estimated from their peak areas using parametric spectral modeling software [46]. The S_{ijk}-s were scaled into absolute concentrations, C_{ijk}^{vivo}, relative to a 0.5 L sphere of $C_i^{vitro} = 12.5$, 10.0, 3.0 and 7.5 mmol/l NAA, Cr, Cho and mI in water at physiological ionic strength to properly load the coil:

$$C_{ijk}^{vivo} = C_i^{vitro} \cdot \frac{S_{ijk}}{S_{ijR}} \cdot \frac{V_k^{180°}}{V_R^{180°}} \cdot f_i \quad \mathrm{mmol/l}, \tag{1}$$

where S_{ijR} is the sphere's voxels' metabolites' signals, $V_{jk}^{180°}$ and $V_R^{180°}$ the radio-frequency voltages for a nonselective 1 ms $180°$ inversion pulse on the k-th subject and sphere, and f_i a correction factor for in vivo (T_1^{vivo}, T_2^{vivo}) and phantom (T_1^{vitro}, T_2^{vitro}) relaxation time differences for metabolite, i:

$$f_i = \frac{\exp\left(-TE/T_2^{vitro}\right)}{\exp\left(-TE/T_2^{vivo}\right)} \cdot \frac{1 - \exp\left(-TR/T_1^{vitro}\right)}{1 - \exp\left(-TR/T_1^{vivo}\right)}, \tag{2}$$

where 3 T NAA, Cr, Cho and mI $T_1^{vivo} = 1335$, 1263, 1147, 1120 ms and $T_2^{vivo} = 325$, 178, 264, 200 ms were used for gray matter regions-of-interest (ROI)s; 1154, 1224, 1032, 960 ms and 316, 182, 263, 200 ms for the white matter ROI [47–49]. Corresponding values for the phantom were $T_1^{vitro} = 605$, 336, 235, 280 ms and $T_2^{vitro} = 483$, 288, 200, 233 ms.

Correcting for cerebrospinal fluid partial volume

ROIs may also contain CSF (see Figs. 2 and 3) whose metabolite concentrations are below the ^{1}H-MRSI detection threshold [50], leading to metabolite concentration underestimation. To correct for this, we produced CSF masks from the axial, T_2-weighted TSE images using our in-house FireVoxel segmentation software package [51] as described previously [29]. Our software then estimated the CSF fraction, CSF_f, within each voxel as shown in Fig. 2 [26]. Finally, the C_{ijk}^{vivo} [from Eq. (1)] in each ROI voxel was divided by its tissue fraction, $T_f = 1 - CSF_f$.

Regional analyses

The centrum semiovale, caudate head, putamen, thalamus and hippocampus were examined in all animals, pre- (healthy) and post-SIV infection. Each was outlined manually as a ROI on the axial MRI, shown in Fig. 3. Our in-house-written software (Integrated Data Language version 6.3, Research Systems Inc., Boulder, Colorado, USA) then 'zero-filled' the processed 16×16 MRSI matrix to 256×256 and averaged each metabolite's concentrations in all voxels that fell entirely or partially within the outline. Note that although zero-filling does not add new information to the data, it can increase the effective spatial resolution and reduce partial volume effects [39,40].

Statistical analyses

The temporal change in each metabolite for each ROI was computed for each animal as the 'pre-' minus the 'post-' infection level so that a positive change reflected a decline over time. The five-animal sample size was insufficient to permit a nonparametric test of whether there was a change in any metabolite (or NAA/Cr ratio) in any ROI. As a result, the paired sample t test was used to assess the temporal change in each metabolite within each ROI. Significance was tested at the $P < 0.05$ level and SAS version 9.0 (SAS Institute, Cary, North Carolina, USA) was used for all calculations.

Results

An example of the VOI position, size and spectra pre- and 4 weeks post-SIV infection is shown in Fig. 1. Shimming yielded a consistent voxel FWHM linewidth, determined by the spectral modeling software, of 5.9 ± 0.9 Hz (mean $\pm$ SD) over the 2240 voxels (224 voxels/scan $\times$ 2 scans/animal $\times$ 5 animals). The SNRs, estimated as each metabolite's peak-height divided by the root-mean-square of the noise, were: NAA $= 25 \pm 8$, Cr $= 16 \pm 6$, Cho $= 10 \pm 3$ and mI $= 10 \pm 4$, leading to reliable fits as reflected by mean voxel Cramer-Rao lower bounds (CRLBs) below 15%. To optimize the analyses' reliability, ROI voxels were included only if their CRLBs were less than 20% for all four metabolites.

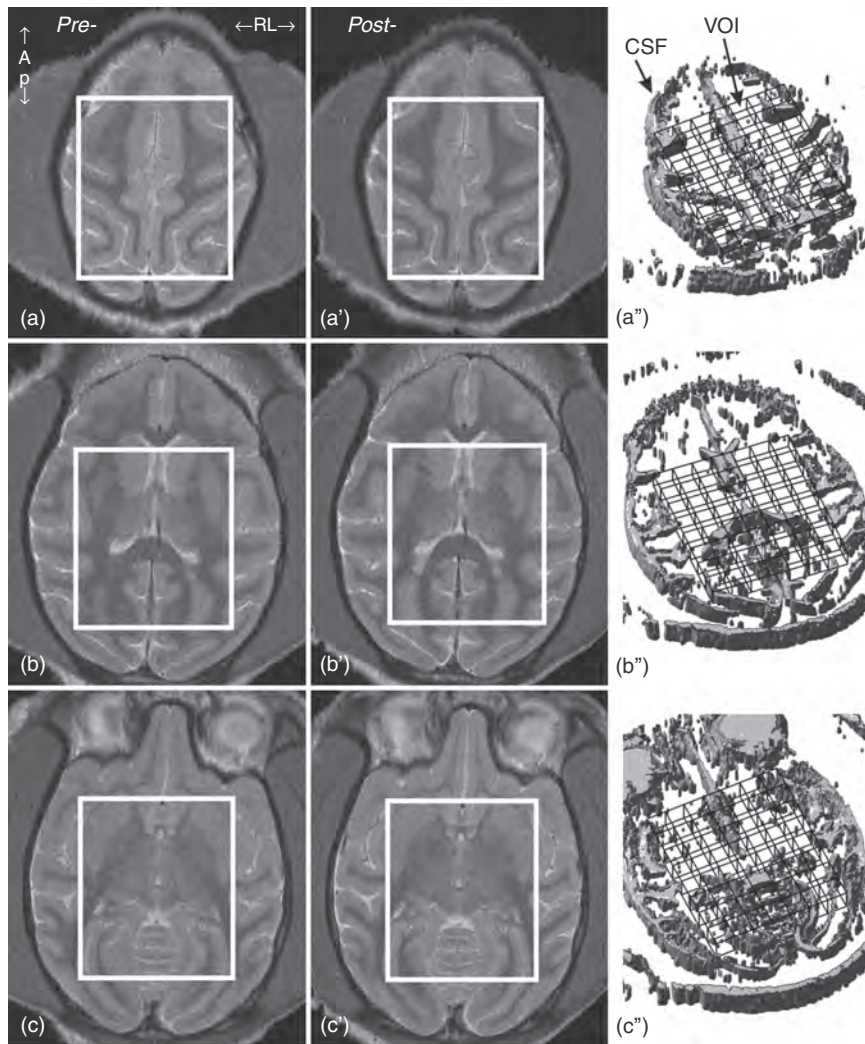An example of each ROI outline is provided in Fig. 3 for a female macaque brain at pre-infection (animal #5 on

Fig. 2. Left (a, b, c); and middle (a′, b′, c′): Axial T_2-weighted MRI showing the 3.5×4.0 cm^2 in-plane relative location and size of the VOI (thick white frame), *pre-* (left) and four weeks *post*-SIV infection in the same animal. Note the VOI placement reproducibility and lack of detectable MRI brain lesions and atrophy. Right (a″, b″, c″): CSF partial volumes (beige) in ^{1}H-MR spectroscopic slices corresponding to the approximate locations of (a′, b′, c′). Four FireVoxel-generated CSF masks (from the MRI) that overlap each 0.5 cm thick ^{1}H-MRSI slice (*cf.* Figure 1) are superimposed over the CSI grid. Each voxel's metabolite values are corrected for CSF partial volume with multiplication by a factor, $1/(1\text{-CSF}_f)$.

Table 1). Metabolite concentrations for every ROI and animal, *pre-* and *post*-SIV infection, are compiled in Table 1 and shown as line-plots in Fig. 4. *Pre-* to *post*-infection mean Cr increased 11% in the thalamus; while *m*I increased 29, 27, 24 and 29% in the centrum semiovale, caudate, thalamus and hippocampus (all $P < 0.05$). Slight increases at the trend level ($P \leq 0.1$) were also observed for Cr in the caudate ($+17\%$) and for *m*I in the putamen ($+24\%$). Neither NAA nor Cho changed significantly. To be consistent with past ^{1}H-MRS studies in this model system we also obtained the NAA/Cr ratio, which is often used for quantification. *Pre-* to *post*-infection mean NAA/Cr declined from 1.02 ± 0.08 to 0.98 ± 0.07 in the centrum semiovale, 0.65 ± 0.03 to 0.53 ± 0.07 in the caudate

and 0.99 ± 0.12 to 0.87 ± 0.07 in the thalamus (-4, -18 and -13%, all $P < 0.05$).

Discussion

Resurgence of more neurovirulent HIV strains, increased drug resistance and higher neurotoxicity associated with prolonged HAART [52,53] underscore the need for noninvasive laboratory markers of HAND pathology for monitoring disease progression. Although an earlier study found global gray matter and white matter ^{1}H-MRSI abnormalities in the brains of these same animals [29], that approach was unable to distinguish multifocal from truly
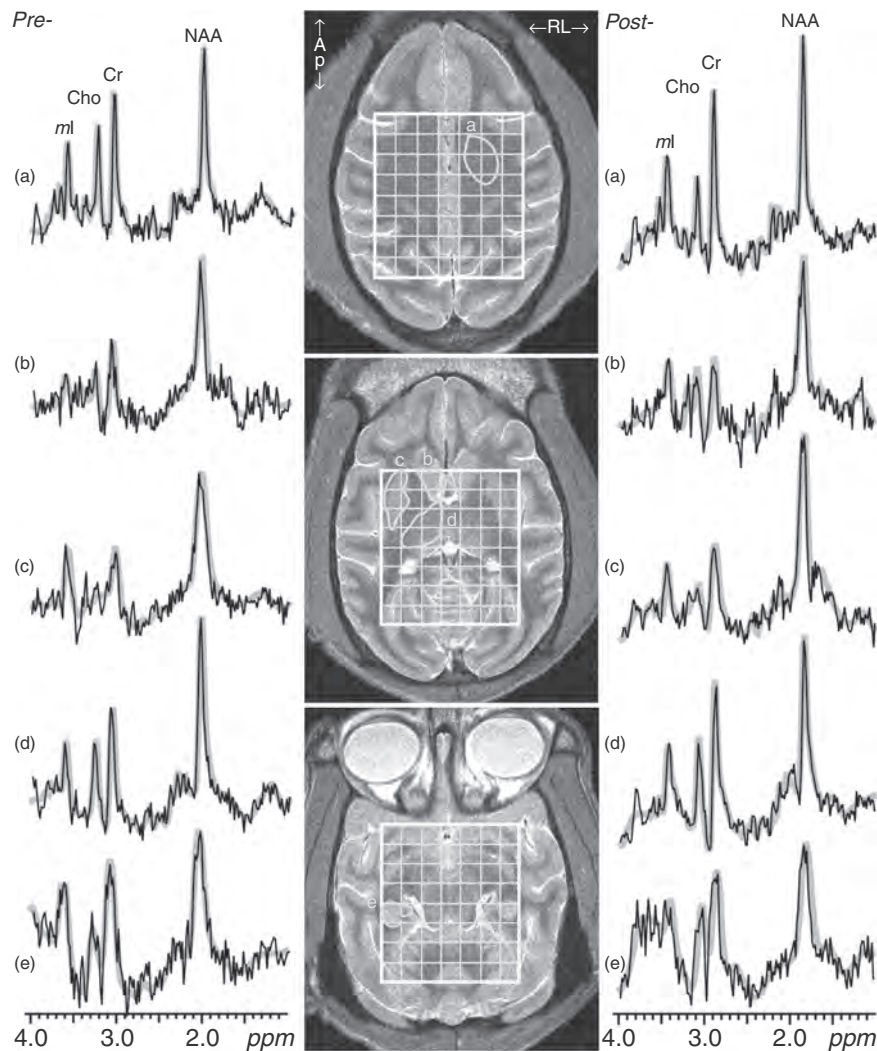
Fig. 3. Left: Real part of the *pre*-SIV infection ¹H spectra averages from all voxels fully or partially within the outlined regions-of-interest (ROI)s (thin black line), superimposed over their fits (thick gray line) for animal #5 in Table 1. Spectra are on the same frequency and intensity scales. Note the improved ROI SNRs (as compared to the single-voxel spectra in Fig. 1) that lead to good spectral fits, as reflected by mean CRLBs of <20% for all metabolites in all ROIs examined. Middle: Axial T_2-weighted MRI showing the volume-of-interest (thick white frame), 7×8 axial-native CSI grid (thin white lines) and ROIs (yellow outlines): **(a)** centrum semiovale, **(b)** caudate (head) nucleus, **(c)** putamen, **(d)** thalamus and **(e)** hippocampus. Note the relationship between the spatial resolution of the grid and the sizes of these ROIs. Right: Same as 'Left' except taken four weeks *post*-SIV infection.

diffuse pathology. Fortunately, the original, high-spatial resolution ¹H-MRSI data facilitates *post hoc* analyses of irregularly shaped ROIs [31], as shown in Fig. 3. Consequently, we examined the structure-specific regional changes in these same animals *pre-* and 4–6 weeks *post-*infection.

Taken together, the findings of both studies suggest that SIV-infection may indeed produce multifocal pathology. First, while global white matter NAA has been shown to decline [29], no NAA decline is seen here in the centrum semiovale (*cf.* Figure 4). Second, although no global gray matter or white matter *m*I elevation was seen previously [29], it is detected here in several individual gray matter

structures and in the centrum semiovale (Table 1 and Fig. 4). Lastly, despite undetected NAA decline in the VOI's deep gray matter structures, histopathology in other rhesus macaques has shown neuronal dysfunction/loss in cortical regions *outside* of our ¹H-MRSI VOI [25,30]. Moreover, immunohistochemistry markers of astrogliosis and neuronal integrity, glial fibrillary acidic protein (GFAP), synaptophysin and microtubule-associated protein 2, along with neuronal counts in animals of the same cohort have shown evidence of variable disease activity in frontal and parietal cortices as well as a pathology gradient in frontal cortex between 4 and 8 weeks *post*-infection, suggesting greater neurodegeneration and gliosis later in the disease [25,30].

Table 1. Metabolic data (mean $\pm$ SD) for each region-of-interest (ROI) of animals #1–5, 'pre-' and 'post-' SIV infection, for each metabolite (NAA, Cr, Cho, *m*I).

ROI	Animal #	NAA[a] pre-	NAA[a] post-	Cr[a] pre-	Cr[a] post-	Cho[a] pre-	Cho[a] post-	*m*I[a] pre-	*m*I[a] post-
Centrum semiovale	1	5.5	5.6	4.9	5.3	1.0	1.1	4.2	5.3
	2	7.0	6.1	7.5	6.8	0.8	0.8	5.1	6.3
	3	5.8	6.3	5.3	6.0	1.0	0.9	5.9	6.8
	4	5.0	5.8	5.2	6.2	0.9	0.9	4.4	7.5
	5	5.1	5.9	5.2	6.3	0.8	0.9	5.7	6.9
	Mean $\pm$ SD	5.7 $\pm$ 0.8	6.0 $\pm$ 0.3	5.6 $\pm$ 1.1	6.1 $\pm$ 0.6	0.9 $\pm$ 0.1	0.9 $\pm$ 0.1	5.1 $\pm$ 0.8	6.6 $\pm$ 0.8*
Caudate	1	5.5	5.0	9.0	9.3	1.9	2.1	6.0	7.7
	2	5.5	4.3	8.7	10.1	1.8	1.8	5.6	7.0
	3	4.0	5.5	5.8	9.8	1.8	2.4	5.8	7.0
	4	5.6	5.0	8.7	9.5	2.4	1.9	4.7	6.8
	5	5.3	5.2	7.9	8.4	2.1	2.1	6.7	7.9
	Mean $\pm$ SD	5.2 $\pm$ 0.7	5.0 $\pm$ 0.5	8.0 $\pm$ 1.3	9.4 $\pm$ 0.6	2.0 $\pm$ 0.2	2.0 $\pm$ 0.2	5.7 $\pm$ 0.7	7.3 $\pm$ 0.5*
Putamen	1	6.7	7.2	9.4	10.1	1.4	1.6	6.1	6.4
	2	6.5	5.3	8.3	7.3	1.1	1.6	5.3	7.0
	3	6.2	6.7	9.0	9.6	1.3	1.3	6.2	6.7
	4	6.0	5.4	6.9	7.1	1.0	1.1	5.5	8.7
	5	6.5	5.9	8.9	8.9	1.3	1.2	5.4	6.5
	Mean $\pm$ SD	6.4 $\pm$ 0.3	6.1 $\pm$ 0.8	8.5 $\pm$ 1.0	8.6 $\pm$ 1.3	1.2 $\pm$ 0.2	1.3 $\pm$ 0.2	5.7 $\pm$ 0.4	7.1 $\pm$ 1.0
Thalamus	1	7.3	7.3	7.0	7.9	1.9	1.9	7.3	7.9
	2	7.9	6.6	6.8	7.4	1.7	1.8	5.9	7.7
	3	7.5	7.3	7.7	8.9	1.9	1.9	7.8	8.9
	4	6.5	6.8	7.5	8.8	1.6	1.9	6.9	9.5
	5	6.5	6.4	7.2	7.0	1.7	1.7	6.2	8.2
	Mean $\pm$ SD	7.2 $\pm$ 0.6	6.9 $\pm$ 0.4	7.2 $\pm$ 0.4	8.0 $\pm$ 0.8*	1.8 $\pm$ 0.1	1.9 $\pm$ 0.1	6.8 $\pm$ 0.8	8.5 $\pm$ 0.8*
Hippocampus	1	–	–	–	–	–	–	–	–
	2	6.9	7.8	6.5	9.1	1.0	1.3	6.2	9.8
	3	7.7	6.8	7.3	6.4	1.1	0.8	7.3	10.4
	4	7.2	6.7	7.1	5.7	1.3	0.7	8.5	10.0
	5	8.2	6.1	7.4	5.4	1.3	0.8	8.7	9.4
	Mean $\pm$ SD	7.7 $\pm$ 1.0	6.8 $\pm$ 0.7	7.1 $\pm$ 0.4	6.7 $\pm$ 1.7	1.2 $\pm$ 0.2	0.9 $\pm$ 0.3	7.7 $\pm$ 1.2	9.9 $\pm$ 0.4*

NAA, *N*-acetylaspartate; Cr, creatine; Cho, choline; *m*I, *myo*-inositol. A '-' indicates data was excluded due to metabolic Cramer-Rao lower bounds > 20%.
[a]Absolute average ROI concentration [mmol/g wet weight].
*$P < 0.05$.

Several explanations could account for such regional and temporal variations: First, various mechanisms may cause different types of damage in different regions, for example, those in the basal ganglia, white matter and parietal cortex [54], as part of a 'multihit' hypothesis; second, damage mechanisms may be similar, but more aggressive in some regions, for example, in the thalamus, due to heavier viral loads; and third, there may be a spatiotemporal dependence, that is, injury begins in one area (which sustains the most damage) and spreads over time to other areas perhaps through Wallerian degeneration. None of these hypotheses was tested in a previous ^{1}H-MRSI study that examined only global abnormalities [29], nor with histopathology since it cannot follow-up the same animal.

Our study demonstrates that ^{1}H-MRSI can identify structure-specific changes: specifically, we found that SIV-infection produces increases in *m*I and Cr, reflecting glial activation, in the thalamus and likely also in the caudate, centrum semiovale and hippocampus. Elevated *m*I in multiple regions is consistent with previous neuropathology in this animal model [25,30], showing widespread elevations of GFAP and ionized calcium binding adaptor molecule 1 – an immunohistochemistry marker of microglial activation – at 4 and 8 weeks *post*-infection. Unchanged NAA, however, suggests that the structures' neuronal cell bodies may (still) be spared. One implication of this is that astrocyte and microglial activation may precede neuropathogenesis, a conclusion consistent with our previous ^{1}H-MRSI finding of elevated global *m*I in the larger (28 cm^3) VOI, along with WM NAA decline (axonal pathology), but no gray matter NAA (neuronal cell body) change in these same SIV-infected macaques [29].

An alternative possibility is that neurons may have been injured earlier [25], but partially recovered because of host immune activation, suggesting a reversible injury coincident with monocyte–associated levels of viremia [55]. It is also noteworthy that although Ratai *et al.* [25] reported significant declines in the NAA/Cr ratio in parietal and frontal cortices that correlated with histopathological declines in synaptophysin and neuronal counts, neither NAA nor Cr change by itself was significant at 4 or 6 weeks *post*-SIV infection.
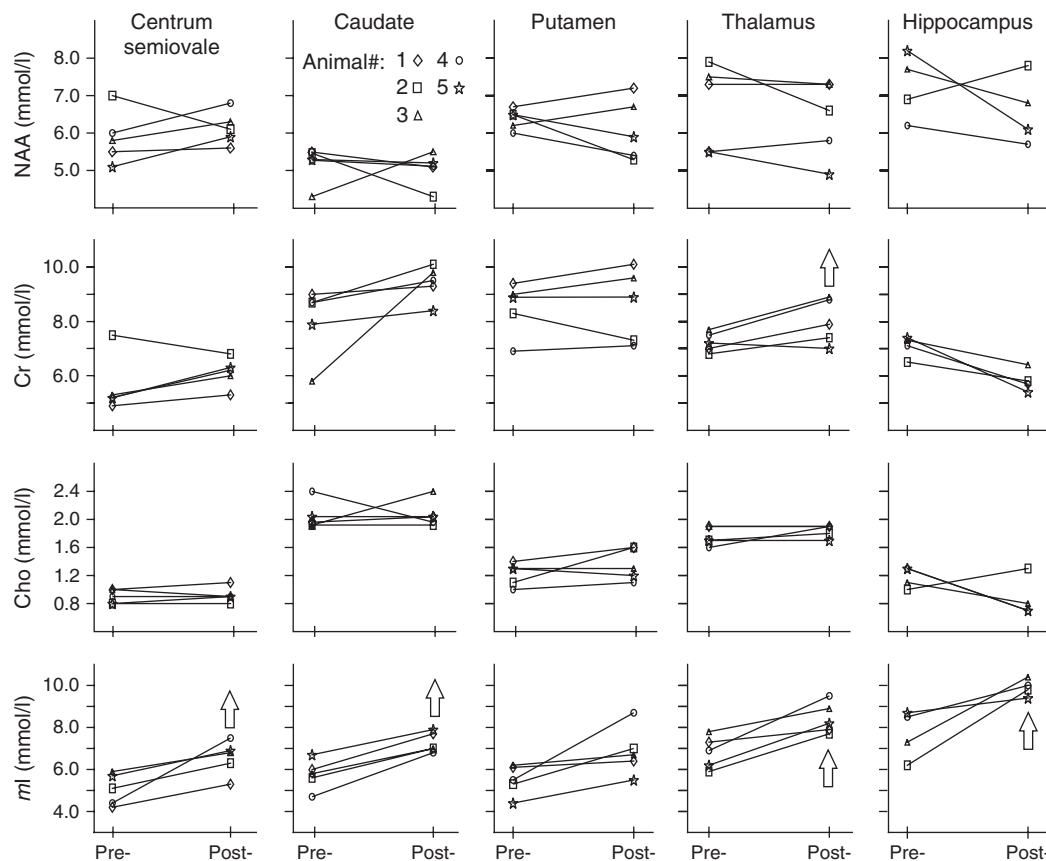
Fig. 4. Line-plots of the *N*-acetylaspartate (NAA), creatine (Cr), choline (Cho) and *myo*-inositol (*m*I) concentration changes from 'Pre-' to 'Post-' SIV infection scans in every region-of-interest for each of the five animals (#1–5, corresponding to Table 1). Note the statistically significant increase in thalamus Cr, as well as significant elevations in *m*I for centrum semiovale, caudate, thalamus and hippocampus (denoted by open arrows).

It is also worth mentioning that metabolite ratios (often to the Cr level) are a common approach to metabolic quantification. Ratios cancel unknown multiplicative factors, for example, static, B_0, and radio-frequency, B_1, field inhomogeneities, instrumental gain, scanner and localization method differences, as well as CSF partial volume, at the cost of noise propagation from the numerator and denominator [56]. Indeed, consistent with previous reports [25,55], our data also yields significant NAA/Cr declines in the centrum semiovale, caudate and thalamus. These reflect coherent decreases in the NAA simultaneous with increased Cr concentrations, as shown in Fig. 4, that are each not quite statistically significant in and of itself. The previously reported global white matter NAA decline [29], together with the centrum semiovale NAA/Cr decline here, may suggest diffuse axonal pathology imparted by Wallerian degeneration [57,58], leading to direct injury of cortical cell bodies that are outside of our ^{1}H-MRSI VOI (see limitation below).

Admittedly, this study is also subject to several limitations: First, due to the proximity of frontal regions to air–tissue interfaces, for example, the paranasal sinuses, which cause

severe B_0 field inhomogeneity [59], our VOI excluded most of the frontal lobes, an area known to be affected in HAND. Second, to avoid lipid contamination our VOI was limited in cortical coverage to midline cortex, missing ∼85−90% of the cortical gray matter. Third, cost constraints limited follow-up of these animals, which had been participating in a longitudinal antiretroviral study, to just five animals, all of which were accelerated models to speed disease progression to terminal AIDS and SIV encephalitis in several months versus years with the traditional SIV model. It is noteworthy that the traditional model may be preferred for its proven ability to recapitulate HIV cerebral pathology, but this requires prohibitively long wait periods. Moreover, the limited number of animals restricted the statistical power, reflected by coefficients of variation (SD/mean) for the ROIs' metabolite concentrations of 9, 12, 12 and 13% for the NAA, Cr, Cho and *m*I, respectively. Logistics notwithstanding, future studies might benefit from more animals scanned later at multiple timepoints to reveal how the disease evolves into its terminal phase.

SIV-infection at this stage appears to cause glial activation, while neuronal cell bodies in the deep gray matter

structures remain relatively spared, or, alternatively, may have already recovered. Treatment regimens to reduce gliosis, therefore, may prove beneficial in preventing downstream neurodegeneration and perhaps ward off neurocognitive impairments. These results also suggest possible relationships between particular brain regions and progressive brain injury, a link that if substantiated would support the hypothesis that more vulnerable regions are 'hit' first, or more aggressively, and disease spreads to other areas only subsequently. Such regional disease heterogeneity and spatiotemporal escalation could be monitored with ¹H-MRSI as a noninvasive, non-destructive alternative to histopathology. Provided that animal testing demonstrates safety, future HIV treatment studies might benefit from anti-inflammatory regimens geared towards reducing gliosis as a strategy against HAND.

Acknowledgements

Conflicts of interest
None of the authors has a conflict of interest.

References

1. Heaton RK, Franklin DR, Ellis RJ, McCutchan JA, Letendre SL, Leblanc S, et al. **HIV-associated neurocognitive disorders before and during the era of combination antiretroviral therapy: differences in rates, nature, and predictors.** *J Neurovirol* 2011; **17**:3–16.
2. Antinori A, Arendt G, Becker JT, Brew BJ, Byrd DA, Cherner M, et al. **Updated research nosology for HIV-associated neurocognitive disorders.** *Neurology* 2007; **69**:1789–1799.
3. Valcour VG, Shikuma CM, Watters MR, Sacktor NC. **Cognitive impairment in older HIV-1-seropositive individuals: prevalence and potential mechanisms.** *AIDS* 2004; **18 (Suppl 1)**: S79–S86.
4. Sacktor N, McDermott MP, Marder K, Schifitto G, Selnes OA, McArthur JC, et al. **HIV-associated cognitive impairment before and after the advent of combination therapy.** *J Neurovirol* 2002; **8**:136–142.
5. Cohen RA, Harezlak J, Gongvatana A, Buchthal S, Schifitto G, Clark U, et al. **Cerebral metabolite abnormalities in human immunodeficiency virus are associated with cortical and subcortical volumes.** *J Neurovirol* 2010; **16**:435–444.
6. Tozzi V, Balestra P, Bellagamba R, Corpolongo A, Salvatori MF, Visco-Comandini U, et al. **Persistence of neuropsychologic deficits despite long-term highly active antiretroviral therapy in patients with HIV-related neurocognitive impairment: prevalence and risk factors.** *J Acquir Immune Defic Syndr* 2007; **45**:174–182.
7. McArthur JC, McDermott MP, McClernon D, St Hillaire C, Conant K, Marder K, et al. **Attenuated central nervous system infection in advanced HIV/AIDS with combination antiretroviral therapy.** *Arch Neurol* 2004; **61**:1687–1696.
8. Sevigny JJ, Albert SM, McDermott MP, Schifitto G, McArthur JC, Sacktor N, et al. **An evaluation of neurocognitive status and markers of immune activation as predictors of time to death in advanced HIV infection.** *Arch Neurol* 2007; **64**:97–102.
9. Gongvatana A, Schweinsburg BC, Taylor MJ, Theilmann RJ, Letendre SL, Alhassoon OM, et al. **White matter tract injury and cognitive impairment in human immunodeficiency virus-infected individuals.** *J Neurovirol* 2009; **15**:187–195.
10. Thompson PM, Dutton RA, Hayashi KM, Toga AW, Lopez OL, Aizenstein HJ, et al. **Thinning of the cerebral cortex visualized in HIV/AIDS reflects CD4+ T lymphocyte decline.** *Proc Natl Acad Sci U S A* 2005; **102**:15647–15652.
11. Cohen RA, Harezlak J, Schifitto G, Hana G, Clark U, Gongvatana A, et al. **Effects of nadir CD4 count and duration of human immunodeficiency virus infection on brain volumes in the highly active antiretroviral therapy era.** *J Neurovirol* 2010; **16**:25–32.
12. Chang L, Ernst T, Witt MD, Ames N, Gaiefsky M, Miller E. **Relationships among brain metabolites, cognitive function, and viral loads in antiretroviral-naive HIV patients.** *Neuroimage* 2002; **17**:1638–1648.
13. Moore DJ, Masliah E, Rippeth JD, Gonzalez R, Carey CL, Cherner M, et al. **Cortical and subcortical neurodegeneration is associated with HIV neurocognitive impairment.** *AIDS* 2006; **20**:879–887.
14. Kure K, Weidenheim KM, Lyman WD, Dickson DW. **Morphology and distribution of HIV-1 gp41-positive microglia in subacute AIDS encephalitis. Pattern of involvement resembling a multisystem degeneration.** *Acta Neuropathol* 1990; **80**:393–400.
15. Archibald SL, Masliah E, Fennema-Notestine C, Marcotte TD, Ellis RJ, McCutchan JA, et al. **Correlation of in vivo neuroimaging abnormalities with postmortem human immunodeficiency virus encephalitis and dendritic loss.** *Arch Neurol* 2004; **61**:369–376.
16. Kruman II, Nath A, Mattson MP. **HIV-1 protein Tat induces apoptosis of hippocampal neurons by a mechanism involving caspase activation, calcium overload, and oxidative stress.** *Exp Neurol* 1998; **154**:276–288.
17. Petito CK, Roberts B, Cantando JD, Rabinstein A, Duncan R. **Hippocampal injury and alterations in neuronal chemokine co-receptor expression in patients with AIDS.** *J Neuropathol Exp Neurol* 2001; **60**:377–385.
18. Sa MJ, Madeira MD, Ruela C, Volk B, Mota-Miranda A, Paula-Barbosa MM. **Dendritic changes in the hippocampal formation of AIDS patients: a quantitative Golgi study.** *Acta Neuropathol* 2004; **107**:97–110.
19. Desrosiers RC. **The simian immunodeficiency viruses.** *Annu Rev Immunol* 1990; **8**:557–578.
20. Murray EA, Rausch DM, Lendvay J, Sharer LR, Eiden LE. **Cognitive and motor impairments associated with SIV infection in rhesus monkeys.** *Science* 1992; **255**:1246–1249.
21. Burudi EM, Fox HS. **Simian immunodeficiency virus model of HIV-induced central nervous system dysfunction.** *Adv Virus Res* 2001; **56**:435–468.
22. Zink MC, Amedee AM, Mankowski JL, Craig L, Didier P, Carter DL, et al. **Pathogenesis of SIV encephalitis. Selection and replication of neurovirulent SIV.** *Am J Pathol* 1997; **151**: 793–803.
23. Greco JB, Westmoreland SV, Ratai EM, Lentz MR, Sakaie K, He J, et al. **In vivo 1H MRS of brain injury and repair during acute SIV infection in the macaque model of neuroAIDS.** *Magn Reson Med* 2004; **51**:1108–1114.

24. Fuller RA, Westmoreland SV, Ratai E, Greco JB, Kim JP, Lentz MR, *et al*. **A prospective longitudinal in vivo 1H MR spectroscopy study of the SIV/macaque model of neuroAIDS.** *BMC Neurosci* 2004; **5**:10.

25. Ratai EM, Annamalai L, Burdo T, Joo CG, Bombardier JP, Fell R, *et al*. **Brain creatine elevation and N-Acetylaspartate reduction indicates neuronal dysfunction in the setting of enhanced glial energy metabolism in a macaque model of neuroAIDS.** *Magn Reson Med* 2011; **66**:625–634.

26. Tal A, Kirov II, Grossman RI, Gonen O. **The role of gray and white matter segmentation in quantitative proton MR spectroscopic imaging.** *NMR Biomed* 2012; **25**:1392–1400.

27. Cheverud JM, Falk D, Vannier M, Konigsberg L, Helmkamp RC, Hildebolt C. **Heritability of brain size and surface features in rhesus macaques (Macaca mulatta).** *J Hered* 1990; **81**:51–57.

28. Goelman G, Liu S, Hess D, Gonen O. **Optimizing the efficiency of high-field multivoxel spectroscopic imaging by multiplexing in space and time.** *Magn Reson Med* 2006; **56**:34–40.

29. Wu WE, Tal A, Kirov II, Rusinek H, Charytonowicz D, Babb JS, *et al*. **Global gray and white matter metabolic changes after simian immunodeficiency virus infection in CD8-depleted rhesus macaques: proton MRS imaging at 3 T.** *NMR Biomed* 2013; **26**:480–488.

30. Ratai EM, Bombardier JP, Joo CG, Annamalai L, Burdo TH, Campbell J, *et al*. **Proton magnetic resonance spectroscopy reveals neuroprotection by oral minocycline in a nonhuman primate model of accelerated NeuroAIDS.** *PLoS One* 2010; **5**:e10523.

31. Hardy CJ, Tal A, Babb JS, Perry NN, Messinger JW, Antonius D, *et al*. **Multivoxel proton MR spectroscopy used to distinguish anterior cingulate metabolic abnormalities in patients with schizophrenia.** *Radiology* 2011; **261**:542–550.

32. Soares DP, Law M. **Magnetic resonance spectroscopy of the brain: review of metabolites and clinical applications.** *Clin Radiol* 2009; **64**:12–21.

33. Williams K, Alvarez X, Lackner AA. **Central nervous system perivascular cells are immunoregulatory cells that connect the CNS with the peripheral immune system.** *Glia* 2001; **36**:156–164.

34. Williams KC, Hickey WF. **Central nervous system damage, monocytes and macrophages, and neurological disorders in AIDS.** *Annu Rev Neurosci* 2002; **25**:537–562.

35. Centers for Disease Control C. **Previous HIV testing among adults and adolescents newly diagnosed with hiv infection: National HIV Surveillance System, 18 Jurisdictions, United States, 2006–2009.** *MMWR* 2012; **61**:441–445.

36. Brew BJ, Crowe SM, Landay A, Cysique LA, Guillemin G. **Neurodegeneration and ageing in the HAART era.** *J Neuroimmun Pharmacol* 2009; **4**:163–174.

37. Zink MC, Clements JE. **A novel simian immunodeficiency virus model that provides insight into mechanisms of human immunodeficiency virus central nervous system disease.** *J Neurovirol* 2002; **8** (Suppl 2):42–48.

38. Schmitz JE, Simon MA, Kuroda MJ, Lifton MA, Ollert MW, Vogel CW, *et al*. **A nonhuman primate model for the selective elimination of CD8+ lymphocytes using a mouse-human chimeric monoclonal antibody.** *Am J Pathol* 1999; **154**:1923–1932.

39. Gonzalez RG, Cheng LL, Westmoreland SV, Sakaie KE, Becerra LR, Lee PL, *et al*. **Early brain injury in the SIV-macaque model of AIDS.** *AIDS* 2000; **14**:2841–2849.

40. Wu WE, Kirov II, Zhang K, Babb JS, Joo CG, Ratai EM, *et al*. **Cross-sectional and longitudinal reproducibility of rhesus macaque brain metabolites: a proton MR spectroscopy study at 3 T.** *Magn Reson Med* 2011; **65**:1522–1531.

41. Goelman G, Liu S, Fleysher R, Fleysher L, Grossman RI, Gonen O. **Chemical-shift artifact reduction in Hadamard-encoded MR spectroscopic imaging at high (3T and 7T) magnetic fields.** *Magn Reson Med* 2007; **58**:167–173.

42. Brooker HR, Mareci TH, Mao JT. **Selective Fourier transform localization.** *Magn Reson Med* 1987; **5**:417–433.

43. Mareci T, Brooker H. **Essential considerations for spectral localization using indirect gradient encoding of spatial information.** *J Magn Reson* 1991; **92**:229–246.

44. Goelman G, Liu S, Gonen O. **Reducing voxel bleed in Hadamard-encoded MRI and MRS.** *Magn Reson Med* 2006; **55**:1460–1465.

45. Marion D, Ikura M, Bax A. **Improved solvent suppression in one- and two-dimensional NMR spectra by convolution of time domain data.** *J Magn Reson* 1989; **84**:425–430.

46. Soher BJ, Young K, Govindaraju V, Maudsley AA. **Automated spectral analysis III: application to in vivo proton MR spectroscopy and spectroscopic imaging.** *Magn Reson Med* 1998; **40**:822–831.

47. Liu S, Gonen O, Fleysher R, Fleysher L, Babb JS, Soher BJ, *et al*. **Metabolite proton T(2) mapping in the healthy rhesus macaque brain at 3 T.** *Magn Reson Med* 2009; **62**:1292–1299.

48. Liu S, Fleysher R, Fleysher L, Joo CG, Ratai EM, Gonzalez RG, *et al*. **Brain metabolites B1-corrected proton T1 mapping in the rhesus macaque at 3 T.** *Magn Reson Med* 2010; **63**:865–871.

49. Posse S, Otazo R, Caprihan A, Bustillo J, Chen H, Henry PG, *et al*. **Proton echo-planar spectroscopic imaging of J-coupled resonances in human brain at 3 and 4 Tesla.** *Magn Reson Med* 2007; **58**:236–244.

50. Lynch J, Peeling J, Auty A, Sutherland GR. **Nuclear magnetic resonance study of cerebrospinal fluid from patients with multiple sclerosis.** *Can J Neurol Sci* 1993; **20**:194–198.

51. Mikheev A, Nevsky G, Govindan S, Grossman R, Rusinek H. **Fully automatic segmentation of the brain from T1-weighted MRI using Bridge Burner algorithm.** *J Magn Reson Imaging* 2008; **27**:1235–1241.

52. Langford TD, Letendre SL, Larrea GJ, Masliah E. **Changing patterns in the neuropathogenesis of HIV during the HAART era.** *Brain Pathol* 2003; **13**:195–210.

53. Cysique LA, Brew BJ. **Neuropsychological functioning and antiretroviral treatment in HIV/AIDS: a review.** *Neuropsychol Rev* 2009; **19**:169–185.

54. Yiannoutsos CT, Ernst T, Chang L, Lee PL, Richards T, Marra CM, *et al*. **Regional patterns of brain metabolites in AIDS dementia complex.** *Neuroimage* 2004; **23**:928–935.

55. Williams K, Westmoreland S, Greco J, Ratai E, Lentz M, Kim WK, *et al*. **Magnetic resonance spectroscopy reveals that activated monocytes contribute to neuronal injury in SIV neuroAIDS.** *J Clin Invest* 2005; **115**:2534–2545.

56. Li BS, Wang H, Gonen O. **Metabolite ratios to assumed stable creatine level may confound the quantification of proton brain MR spectroscopy.** *Magn Reson Imaging* 2003; **21**:923–928.

57. Lexa FJ, Grossman RI, Rosenquist AC. **MR of wallerian degeneration in the feline visual system: characterization by magnetization transfer rate with histopathologic correlation.** *AJNR* 1994; **15**:201–212.

58. Waller A. **Experiments on the section of the glossopharyngeal and hypoglossal nerves of the frog, and observations of the alterations produced thereby in the structure of their primitive fibres.** *Phil Trans R Soc Lond* 1850; **140**:423–429.

59. Duyn JH, Gillen J, Sobering G, van Zijl PC, Moonen CT. **Multisection proton MR spectroscopic imaging of the brain.** *Radiology* 1993; **188**:277–282.